

# A Quasar-Galaxy Mixing Diagram: Quasar Spectral Energy Distribution Shapes in the Optical to Near-Infrared

Heng Hao<sup>1,2\*</sup>, Martin Elvis<sup>1</sup>, Brandon C. Kelly<sup>1</sup>, Francesca Civano<sup>1</sup>, Angela Bongiorno<sup>3,4</sup>, Gianni Zamorani<sup>5</sup>, Annalisa Celotti<sup>2,6</sup>, Luis C. Ho<sup>7</sup>, Andrea Merloni<sup>3</sup>, Knud Jahnke<sup>8</sup>, Andrea Comastri<sup>5</sup>, Jonathan R. Trump<sup>9</sup>, Vincenzo Mainieri<sup>10</sup>, Mara Salvato<sup>11,12</sup>, Marcella Brusa<sup>3</sup>, Chris D. Impey<sup>13</sup>, Anton M. Koekemoer<sup>14</sup>, Giorgio Lanzuisi<sup>3</sup>, Cristian Vignali<sup>5,15</sup>, John D. Silverman<sup>16</sup>, C. Megan Urry<sup>17</sup>, Kevin Schawinski<sup>18</sup>

<sup>1</sup>Harvard-Smithsonian Center for Astrophysics, 60 Garden Street, Cambridge, MA 02138, USA

<sup>2</sup>SISSA, Via Bonomea 265, I-34136 Trieste, Italy

<sup>3</sup>Max Planck Institute für Extraterrestrische Physik, Postfach 1312, 85741, Garching bei München, Germany

<sup>4</sup>INAF-Osservatorio Astronomico di Roma, Via di Frascati 33, 00040, Monteporzio Catone, Rome, Italy

<sup>5</sup>INAF - Osservatorio Astronomico di Bologna, via Ranzani 1, I-40127 Bologna, Italy

<sup>6</sup>INAF - Osservatorio Astronomico di Brera, via E. Bianchi 46, I-23807 Merate, Italy

<sup>7</sup>The Observatories of the Carnegie Institute for Science, Santa Barbara Street, Pasadena, CA 91101, USA

<sup>8</sup>Max-Planck-Institut für Astronomie, Königstuhl 17, Heidelberg, D-69117, Germany

<sup>9</sup>UCO/Lick Observatory, University of California, Santa Cruz, CA 95064, USA

<sup>10</sup>European Southern Observatory, Karl-Schwarzschild-Strasse 2, D-85748 Garching bei München, Germany

<sup>11</sup>IPP - Max-Planck-Institute for Plasma Physics, Boltzmann Strasse 2, D-85748, Garching bei München, Germany

<sup>12</sup>Excellence Cluster, Boltzmann Strasse 2, D-85748, Garching bei München, Germany

<sup>13</sup>Steward Observatory, University of Arizona, 933 North Cherry Avenue, Tucson, AZ 85721, USA

<sup>14</sup>Space Telescope Science Institute, 3700 San Martin Drive, Baltimore, MD 21218, USA

<sup>15</sup>Dipartimento di Astronomia, Università degli Studi di Bologna, Via Ranzani 1, 40127 Bologna, Italy

<sup>16</sup>Institute for the Physics and Mathematics of the Universe (IPMU), University of Tokyo, Kashiwanoha 5-1-5, Kashiwa-shi, Chiba 277-8568, Japan

<sup>17</sup>Physics Department and Yale Center for Astronomy and Astrophysics, Yale University, New Haven, CT 06511, USA

<sup>18</sup>Institute for Astronomy, Department of Physics, ETH Zurich, Wolfgang-Pauli-Strasse 16, CH-8093 Zurich, Switzerland

Version Oct 8th, 2012.

## ABSTRACT

We define the quasar-galaxy mixing diagram by the slopes of the spectral energy distribution (SED) of quasars from  $1\mu\text{m}$  to  $3000\text{ \AA}$  and from  $1\mu\text{m}$  to  $3\text{ }\mu\text{m}$  in the rest frame. The mixing diagram can easily distinguish among quasar-dominated, galaxy-dominated and reddening-dominated SED shapes. By studying the position of the 413 XMM selected Type 1 AGN in the wide-field “Cosmic Evolution Survey” (COSMOS) in the mixing diagram, we find that a combination of the Elvis et al. (1994, hereafter E94) quasar SED with various contributions from galaxy emission and some dust reddening is remarkably effective in describing the SED shape near  $1\mu\text{m}$  for large ranges of redshift, luminosity, black hole mass and Eddington ratio of type 1 AGN. In particular, the location in the mixing diagram of the highest luminosity AGN is very close (within  $1\sigma$ ) to that expected on the basis of the E94 SED. The mixing diagram can also be used to estimate the host galaxy fraction and reddening in the SED. We also show examples of some outliers which might be AGN in different evolutionary stages compared to the majority of AGN in the quasar-host galaxy co-evolution cycle.

**Key words:** galaxies: evolution; quasars: general; surveys

## 1 INTRODUCTION

The masses of the super massive black holes (SMBHs) that exist in most, if not all, galaxy nuclei (e.g. Kormendy &

\* E-mail:henghao@post.harvard.edu

Richstone 1995), are proportional to their host galaxy bulge stellar mass, as measured by either luminosity (Kormendy & Richstone 1995; Marconi & Hunt 2003) or velocity dispersion (Ferrarese & Merritt 2000; Gebhardt et al. 2000). As most SMBH growth occurs during their active phases (the ‘Soltan argument’, Soltan 1982), most bulges must have gone through an active phase, being seen as a quasar or active galactic nucleus (AGN). It is observed that both galaxies and AGN exhibit coordinated “downsizing”: massive galaxy star formation peaks at  $z \sim 2$ , while high luminosity quasars have their peak space density at  $z = 2 - 3$  (Silverman et al. 2005, Brusa et al. 2010, Civano et al. 2011); lower mass galaxies star formation peaks at  $z = 1 - 1.5$ , as do lower luminosity AGN (Franceschini et al. 1999; Ueda et al. 2003; Brandt & Hasinger 2005; Bongiorno et al. 2007). A close co-evolutionary link between SMBH activity and host galaxy evolution seems to be required.

In principle, we could study whatever feedback process controls this co-evolution, by separately analyzing the emission associated to the SMBH and the host galaxy in the same objects. Observationally, however, it is difficult to disentangle the emission from quasar and host galaxy in the optical-IR range, especially for high redshift ( $z > 1$ ) objects. Spatially decomposing a point-source AGN and an extended host requires expensive high-resolution Hubble Space Telescope imaging. Even the  $0.1''$  angular resolution of the Hubble cannot easily resolve the extended host emission from the point-like AGN emission at  $z > 1$ . SED fitting techniques can do so, but have to assume one or several quasar and galaxy SED models (e.g. Merloni et al. 2010), which might lead to systematic errors that are difficult to quantify.

As an alternative approach, we have made use of the fact that the spectral energy distributions (SEDs) of a quasar and of a galaxy near  $1\mu m$  are completely different. Quasar SEDs show a pronounced dip near  $1\mu m$ , while, in contrast, a galaxy SED peaks at around  $1\mu m$ - $2\mu m$ . This dichotomy allows us to define a diagram of near-infrared (NIR) versus optical (OPT) slopes on either side of  $1\mu m$  (rest frame) that cleanly separates the two SED forms.

In this diagram (Figure 1), galaxies lie in a well-defined region ( $\alpha_{\text{OPT}} < 0$ ,  $\alpha_{\text{NIR}} > 0.8$ ), that is clearly distinct from the location of the standard AGN SED ( $\alpha_{\text{OPT}} > 0$ ,  $\alpha_{\text{NIR}} < 0$ , Elvis et al. 1994, hereinafter E94). Reddening moves objects almost perpendicularly to a line joining the galaxy locus to the AGN locus in the diagram. Thus this diagram can distinguish the quasar-dominated, host-dominated or reddening-dominated SEDs easily, without strong model assumptions, and can pick out AGN with mixtures of these three components. Hence we call this the Quasar-Galaxy mixing diagram (hereinafter “mixing diagram” for short).

With this convenient tool, we can more easily study the evolution of quasar SEDs with physical parameters, identify outliers, and estimate host/reddening contributions. This mixing diagram is a generalization of the quasar-galaxy mixing curves in the  $(U-B)(B-V)$  color-color plane defined for “N galaxies” by Sandage (1971) and Weedman (1973). The plot is equivalent to a color-color plot, but utilizes more photometric bands and is defined in the rest frame. As a result, the mixing diagram can be used for sources at any redshift.

In this paper, we use the mixing diagram to study the SED shape in the optical to near-infrared decade ( $3\mu\text{m}$  to  $3000\text{ \AA}$ ) for three type 1 AGN samples: the large XMM-

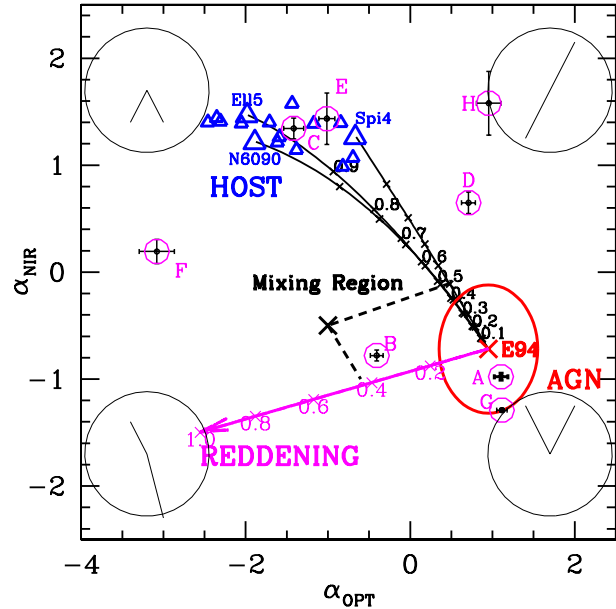


**Figure 1.** The mixing diagram  $\alpha_{\text{NIR}}$  ( $3\mu\text{m}$  to  $1\mu\text{m}$ ) versus  $\alpha_{\text{OPT}}$  ( $1\mu\text{m}$  to  $0.3\mu\text{m}$ ). Note that these slopes are defined in  $\log\nu L_\nu$  versus  $\log\nu$  plane. Different regions of the plot correspond to different SED shapes, as shown in the black circle at the four corners of the plot. The E94 radio-quiet mean SED is shown as a red cross. The red circle shows the dispersion of the quasar samples (§ 3.3). The blue symbols indicate the 16 galaxy templates from “SWIRE Template Library” (Polletta et al. 2007). The black lines connecting the galaxy templates and the E94 mean SED are mixing curves (§ 2.1), showing where the quasar-galaxy mixing SED would locate. The numbers beside the mixing curves are the galaxy fraction. The purple arrow shows the reddening vector applied to the E94 radio-quiet mean SED. The numbers under the reddening vector show the E(B-V) values. The circled points show the position of the outliers in the sample discussed in Elvis et al. (2012) (A, B, C, D) and in § 4.4 of this paper (E, F, G, H).

COSMOS type 1 AGN sample (Elvis et al. 2012, Paper I hereinafter), the SDSS-Spitzer quasar sample (Richards et al. 2006, R06 hereinafter) and the bright quasar sample (E94). Detailed description of the three samples are in § 3.1. We primarily focus on the XMM-COSMOS type 1 AGN sample to demonstrate the major applications of the mixing diagram.

All the wavelengths considered in this paper are in the rest frame. We adopt the WMAP 5-year cosmology (Komatsu et al. 2009), with  $H_0 = 71 \text{ km s}^{-1} \text{ Mpc}^{-1}$ ,  $\Omega_M = 0.26$  and  $\Omega_\Lambda = 0.74$ .

## 2 QUASAR-GALAXY MIXING DIAGRAM

The mixing diagram axes are the  $1 - 3\mu\text{m}$  SED power-law slope ( $\alpha_{\text{NIR}}$ ) versus the  $0.3 - 1\mu\text{m}$  power-law slope ( $\alpha_{\text{OPT}}$ ), where  $\nu F_\nu \propto \nu^\alpha$ . These ranges lie on either side of the  $1\mu\text{m}$  dip, or inflection point, of the rest frame SED.

The  $1\mu\text{m}$  wavelength point is not chosen as the central point arbitrarily. This is where the Wien tail of the black body thermal emission of the hottest dust (at the maximum sublimation temperature of  $\sim 1500$  K, Barvainis et al. 1987)

**Table 1.** Spectral Slopes for different  $f_g$  values (Mixing Curve)

$f_g$	Spi4		Ell5		Sb		S0		NGC6090	
	$\alpha_{\text{OPT}}$	$\alpha_{\text{NIR}}$								
0.0	0.950	-0.719	0.950	-0.719	0.950	-0.719	0.950	-0.719	0.950	-0.719
0.1	0.876	-0.621	0.857	-0.618	0.862	-0.617	0.860	-0.617	0.864	-0.620
0.2	0.794	-0.513	0.752	-0.506	0.762	-0.506	0.759	-0.506	0.766	-0.511
0.3	0.702	-0.394	0.634	-0.382	0.648	-0.383	0.641	-0.383	0.655	-0.392
0.4	0.598	-0.262	0.496	-0.244	0.515	-0.246	0.505	-0.245	0.525	-0.260
0.5	0.480	-0.112	0.334	-0.086	0.357	-0.090	0.341	-0.089	0.372	-0.111
0.6	0.342	0.060	0.138	0.097	0.164	0.089	0.140	0.091	0.184	0.059
0.7	0.178	0.263	-0.109	0.316	-0.082	0.302	-0.119	0.304	-0.053	0.257
0.8	-0.024	0.509	-0.439	0.586	-0.415	0.563	-0.475	0.566	-0.373	0.497
0.9	-0.286	0.823	-0.934	0.941	-0.925	0.902	-1.037	0.906	-0.857	0.800
1.0	-0.656	1.264	-1.972	1.469	-2.044	1.396	-2.447	1.403	-1.876	1.218

begins to outshine the optical band  $\alpha \sim -0.3$  power-law of the SMBH accretion disk (Malkan & Sargent 1982, Sanders et al. 1989, E94, Glikman et al. 2006).

We tried several different wavelength ranges to calculate the slopes and found that these ranges best represent the dip around  $1\mu\text{m}$ . Shorter wavelengths, into the UV, are affected by variability and by the FeII ‘small bump’ (Wills, Netzer & Wills, 1985); longer wavelengths encounter a range of cooler dust emission which adds noise to the NIR slope. In this wavelength range, the XMM-COSMOS type 1 AGN SED dispersion is invariant in a large range of  $z$  and  $L_{\text{bol}}$  (Hao et al. 2012a, Paper II hereinafter), which implies an invariant intrinsic dispersion of SED shape in this wavelength range.

To ensure reliable slopes, we require at least 4 photometric points to define each slope. For the XMM-COSMOS quasar sample, the optical data set is so rich that the mean number of photometry points used in calculating  $\alpha_{\text{OPT}}$  is  $13.1 \pm 5.7$ , while the infrared data is less rich and the mean number of photometry points used in calculating  $\alpha_{\text{NIR}}$  is  $4.1 \pm 0.5$ . The errors on the slopes ( $\alpha_{\text{OPT}}$  and  $\alpha_{\text{NIR}}$ ) are the standard errors of the linear fit.

The major characteristics of the mixing diagram are shown in Figure 1. The E94 radio-quiet (RQ) mean SED template is shown by a red cross. This template is bluer than almost all COSMOS XMM quasars (Paper I), probably due to the (U-B) selection criterion used to select it (Schmidt & Green 1983). The 16 galaxy templates<sup>1</sup> from the “SWIRE Template Library” (Polletta et al. 2007) are shown as blue triangles. Lines joining the E94 mean SED to three representative galaxy templates are drawn. These mixing curves are marked at 10% intervals of host galaxy contribution (see § 2.1 for details).

Note that the slopes are defined in  $\log \nu L_{\nu}$  versus  $\log \nu$  plane. Different SED shapes lie in different regions of the mixing diagram, as sketched inside the circles in the four corners: the *bottom right* corner shows the  $1\mu\text{m}$  inflection of an AGN dominated SED; the *upper left* corner shows the

cool starlight peak of a galaxy dominated SED; the *bottom left* corner shows the rapid drop in the optical characteristics of a dust reddening dominated SED. The *top right* corner shows an SED falling throughout the entire optical-NIR range. This was not a known SED shape until the recent discovery of “hot dust poor” AGN (Jiang et al. 2010; Hao et al. 2010, 2011), which make up 10% of the quasar population (Hao et al. 2011).

## 2.1 Galaxy Fraction Mixing Curves

We can quantify the host galaxy contribution fraction  $f_g$  at  $1\mu\text{m}$  for any quasar, assuming that the E94 RQ template represents a pure AGN SED. A definition similar to  $f_g$  is widely used in SED fitting with different normalization wavelengths (e.g. Salvato et al. 2009, Merloni et al. 2010). The parameter  $f_g$  is defined as the galaxy fraction at  $1\mu\text{m}$ , and describes how close the observed SED is to the galaxy templates. First, we normalize both the galaxy and AGN template at  $1\mu\text{m}$ . Then the mixture of some fraction of galaxy ( $f_g$ ) and some fraction of AGN ( $1-f_g$ ) emission can be calculated accordingly. Suppose that at frequency  $\nu$  the galaxy template SED luminosity is  $\nu L_{\nu}^G$  and the AGN template (E94) SED luminosity is  $\nu L_{\nu}^A$ , then the mixing of the two SEDs luminosity is  $\nu L_{\nu}^{mix} = f_g \nu L_{\nu}^G + (1-f_g) \nu L_{\nu}^A$ .

The black curves in Figure 1 show the slopes of SED templates obtained by mixing the AGN and galaxy templates with values of  $f_g = 0 - 1$ . The mixing curves of the starburst galaxy “NGC6090” and the spiral galaxy “Spi4” define the red and blue boundaries of the possible slopes obtained by mixing the E94 SED with all the 16 galaxy templates in the SWIRE library. The spectral slopes for mixtures of E94 with Spi4, Ell5, Sb, S0, and NGC6090 for 11 values of  $f_g$  are listed in Table 1. The complete table for all the 16 templates is available on line.

## 2.2 Reddening Vector

Intrinsic reddening in AGN is often important in defining their SEDs (e.g., Ward et al. 1987; O’Brien et al. 1988; Young et al. 2008; Shang et al. 2011). The magenta arrow in Figure 1 shows  $\alpha_{\text{OPT}}$  and  $\alpha_{\text{NIR}}$  for the E94 SED when reddened by  $E(\text{B-V}) = 0 - 1$  mag. The reddening of the E94 SED is derived with the IDL de-reddening routine ‘FM\_UNRED.PRO’, which uses the Fitzpatrick (1999) pa-

<sup>1</sup> The 16 galaxy templates in the “SWIRE Template Library” (Polletta et al. 2007) include: 3 elliptical galaxy templates “Ell2”, “Ell5”, “Ell13” representing elliptical galaxy of age 2 Gyr, 5 Gyr and 13 Gyr respectively; 7 spiral galaxy templates “S0”, “Sa”, “Sb”, “Sc”, “Sd”, “Sdm”, “Spi4”; and 6 starburst galaxy templates “NGC6090”, “M82”, “Arp220”, “IRAS20551-4250”, “IRAS22491-1808”, “NGC6240”.

**Table 2.** Reddening Vector

E(B-V)	$\alpha_{\text{OPT}}$	$\alpha_{\text{NIR}}$
0.0	0.950	-0.719
0.1	0.596	-0.798
0.2	0.242	-0.877
0.3	-0.112	-0.956
0.4	-0.465	-1.034
0.5	-0.819	-1.113
0.6	-1.173	-1.192
0.7	-1.527	-1.271
0.8	-1.881	-1.350
0.9	-2.235	-1.428
1.0	-2.588	-1.507

rameterizations with the Small Magellanic Cloud (SMC) extinction curve (Gordon et al. 2003) parameter. The SMC reddening law (Fitzpatrick 1999; Gordon et al. 2003) is typically used for quasars, and is shown to fit reddening in quasars more effectively than a Large Magellanic Cloud (LMC) or Milky Way reddening law (Hopkins et al. 2004; Richards et al. 2003). Reddening primarily affects  $\alpha_{\text{OPT}}$ . The effect of reddening is reported in Table 2.

Using the reddening vector, we can estimate  $f_g$  and E(B-V) from the mixing diagram for sources lying off the E94-host mixing curves toward the lower left. For each source we can draw a line parallel to the reddening curve (black dashed line in Figure 1). The crossing point of this line and the mixing curve shows approximately the value of  $f_g$ . The length of the parallel line gives an estimate of E(B-V). We use this technique in § 4.2 and § 4.3.

Note that different reddening law could cause different  $f_g$  and E(B-V) derived from the mixing diagram. However, Gordon et al. (2003) performed a comparison between SMC, LMC and Milky Way reddening laws and found that the extinction curves only begin to diverge shortward of  $\sim 2000\text{\AA}$  and at rest frame near-UV ( $\sim 2500\text{\AA}$ ) through near infrared ( $\sim 1\mu\text{m}$ ), the three laws are extremely similar. So for the rest frame wavelength range in which the mixing diagram is defined ( $3000\text{\AA}$  to  $1\mu\text{m}$  and  $1\mu\text{m}$  to  $3\mu\text{m}$ ), the results should not be significantly depend on the reddening law. We will only consider the SMC reddening law in the following discussion.

### 3 MIXING DIAGRAM FOR TYPE 1 AGN SAMPLES

#### 3.1 Type 1 AGN Samples

The three type 1 AGN samples we used in this paper are:

(1) The XMM-COSMOS type 1 AGN Sample (XC413, Paper I). The COSMOS field (Scoville et al. 2007) was imaged in X-rays with *XMM-Newton* for a total of  $\sim 1.5$  Ms (Hasinger et al. 2007; Cappelluti et al. 2007, 2009). Optical identifications were made by Brusa et al. (2007, 2010) for the entire XMM-COSMOS sample, who gave photometric properties and redshifts for each X-ray point source. From this complete sample, we extracted a sample of 413 type 1 AGN, defined by having broad line FWHM  $> 2000 \text{ km s}^{-1}$ . The XC413 catalog is described in detail in Paper I.

This sample has full wavelength coverage from radio to

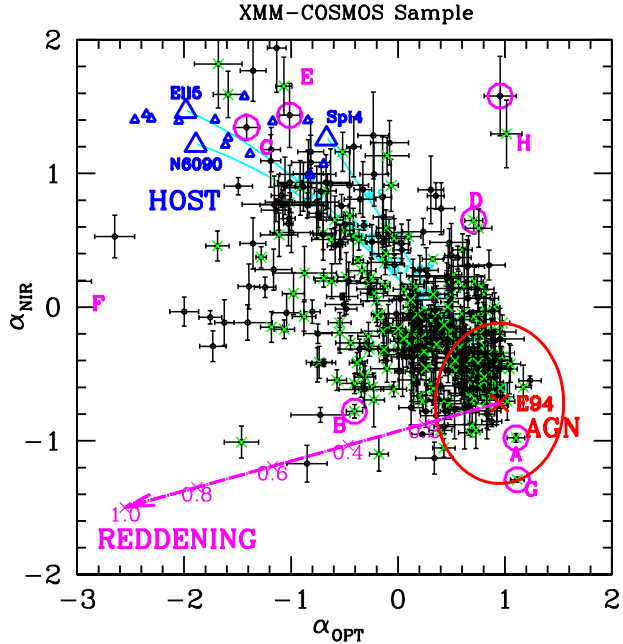


**Figure 2.** The mixing diagram of the XMM-COSMOS type 1 AGN sample (XC413). The other points and lines are color-coded as in Figure 1. The green crosses show the 206 quasars with black hole mass estimates (the SS206 sub-sample, Hao et al. 2012a).

X-ray (for a total of 43 photometric bands, Paper I) and high confidence level spectroscopic redshifts (Trump et al. 2009; Schneider et al. 2007; Lilly et al. 2007, 2009). In this paper, we also added the recently released H band photometry from CFHT/WIRCAM (McCracken et al. 2010). For 405 out of the 413 XMM-COSMOS quasars now have H band photometry, compared to 252 out of 413 in Paper I. The COSMOS type 1 AGN sample has an extremely rich coverage (36 bands) in the optical to near-infrared range. The objects have redshifts  $0.1 \leq z \leq 4.3$  and magnitudes  $16.9 \leq i_{AB} \leq 24.8$ , with 94% - 98% being radio-quiet (Hao et al. 2012b).

In this sample, 206 quasars have published black hole mass measurements (Trump et al. 2009b; Mervoni et al. 2010), which are based on the scaling relationship between BEL FWHM and black hole mass (Vestergaard 2004). For the quasars with only zCOSMOS spectra, the black hole mass was estimated for only the ones with MgII lines in the spectra (Mervoni et al. 2010), using the calibration of McLure & Jarvis (2002). For the rest of the sample, the BELs are located close to the edge of the spectrum, so that reliable black hole mass estimates cannot be made. We call the sub-sample with black hole mass estimates as SS206 hereinafter.

(2) The SDSS-Spitzer Sample (R06). The R06 sample consists of 259 *Spitzer* sources identified with Sloan Digital Sky Survey (SDSS) quasars in four different degree-scale fields, and is, therefore, mid-IR identified and optically selected. The redshift range covered is  $z = 0.14 - 5.2$  with 93% being at  $z < 3$ . Most (215/259) of the R06 sources did not have 2MASS J H K photometry. Details about how we measured the slopes with this sample are described in Hao et al. (2011).

(3) The bright quasar sample (E94). This sample con-

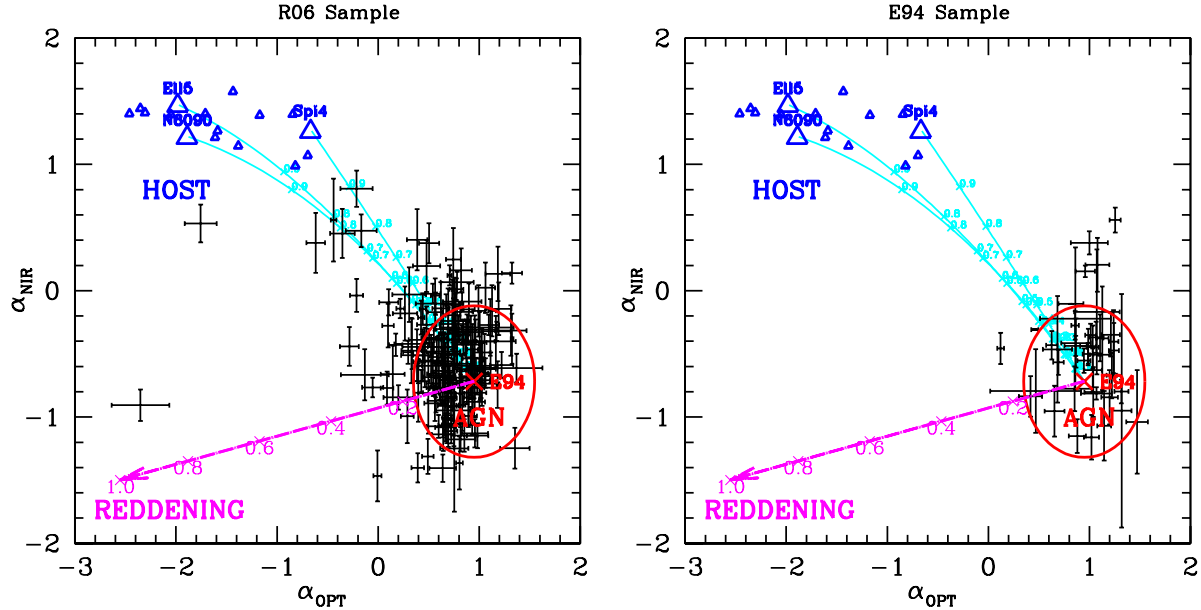


**Figure 3.** The mixing diagram of the SDSS-Spitzer quasar sample (R06, left) and the bright quasar sample (E94, right). The other points and lines are color-coded as in Figure 2.

sists of 42 quasars in the redshift range  $z = 0.025 - 0.94$ , with 80% of them being at  $z < 0.3$ . The optical photometry was obtained at the FLWO (F. L. Whipple Observatory) 24 inch telescope within one week of the MMT FOGS (Faint Object Grism Spectrograph) spectroscopic observations. The NIR data were obtained with MMT and IRTF. More details on the observation can be found in E94. The E94 sample has a bolometric luminosity ( $\log L_{\text{bol}}$ ) in the range of  $44.6 - 47.2$  erg/s with mean of 45.75 erg/s. Note that in this paper we recalculate the bolometric luminosity of the E94 quasars with the same cosmological parameters used for XC413. Compared to XC413, E94 sample is on average more luminous and contains less low luminosity quasars than the XC413. The Eddington ratio of the PG quasar (including E94 sample) is comparable to the XC413 (Sikora et al. 2007, Paper II).

### 3.2 Mixing Diagram for the Type 1 AGN Samples

We plot the XC413 sample on the mixing diagram in Figure 2. The distribution is continuous and largely lies between the E94 mean SED and the galaxy templates, along the mixing curves, with some spread in the reddening direction to values as large as  $E(B-V) \sim 0.6$ , but mostly with  $E(B-V) < 0.3$ . The green crosses represent objects with black hole mass estimates (Paper II), which span the range of the entire sample in the mixing diagram.

The diagram shows that about 90% of the sources lie in the left hand triangular ‘mixing wedge’ between the mixing curves and the reddening vector. The SEDs of all these AGN can be accounted for with a simple combination of an E94 quasar SED, plus a galaxy contribution and reddening. This suggests that the AGN sample is consistent with a single intrinsic SED shape, closely resembling the E94 quasar SED.

For comparison, we also plot the mixing diagram for the SDSS-spitzer quasar sample (R06) and the bright quasar sample (E94), shown in Figure 3 (see also Hao et al. 2011).

For the optically-selected R06 sample, quasars by selection are more clustered in the quasar dominated region unlike the X-ray-selected XC413, which includes more sources with low quasar to host galaxy contrast. The E94 quasars have been corrected for host galaxy contribution. Thus they are by construction clustered around the E94 mean (red cross) in the quasar dominated region. Compared to the E94 sample, the R06 sample is not as blue in optical, probably because E94 is biased towards blue quasars.

### 3.3 Intrinsic Slope Dispersion

We selected a sub-sample of AGN-dominated XC413 SEDs with  $\alpha_{\text{OPT}} > 0.2$  in order to exclude galaxy- or reddening-dominated sources. This sample has a mean slope  $\bar{\alpha}_{\text{OPT}} = 0.61$  (standard deviation  $\sigma_{\text{OPT}} = 0.24$ ), and  $\bar{\alpha}_{\text{NIR}} = -0.29$  (standard deviation  $\sigma_{\text{NIR}} = 0.41$ ). The E94 RQ mean ( $\alpha_{\text{OPT}}(\text{E94}) = 0.95$ ,  $\alpha_{\text{NIR}}(\text{E94}) = -0.72$ , see values in Table 1 for  $f_g = 0$ ) lies at the extreme blue end of the distribution.

To estimate the intrinsic dispersion within the AGN-dominated XC413 sub-sample we removed the effect of measurement error, namely:  $\sigma_{\text{INT}} = \sqrt{\sigma^2 - Err^2}$ . The mean of the measurement error for  $\alpha_{\text{OPT}}$  is  $Err_{\text{OPT}} = 0.11$ , and for  $\alpha_{\text{NIR}}$  is  $Err_{\text{NIR}} = 0.11$ . The intrinsic dispersion thus is  $\sigma_{\text{INT,OPT}} = 0.21$  and  $\sigma_{\text{INT,NIR}} = 0.39$  respectively. Therefore, the intrinsic dispersion of the SED shape is 2 - 4 times the measurement error and seems to be significant.

The equivalent intrinsic dispersions in the E94 and R06 sample were estimated by Hao et al. (2011), who found:  $\sigma_{\text{E94,INT,OPT}} = 0.25$ ,  $\sigma_{\text{E94,INT,NIR}} = 0.32$ ,  $\sigma_{\text{R06,INT,OPT}} = 0.23$ , and  $\sigma_{\text{R06,INT,NIR}} = 0.36$  respectively. The intrinsic dispersions are thus similar for all the three samples.

To compare the intrinsic dispersion of these three samples more rigorously, we applied the Bayesian method of Kelly et al. (2007). This assumes that the intrinsic distribution of the slopes is a mixture of Gaussians. The prob-

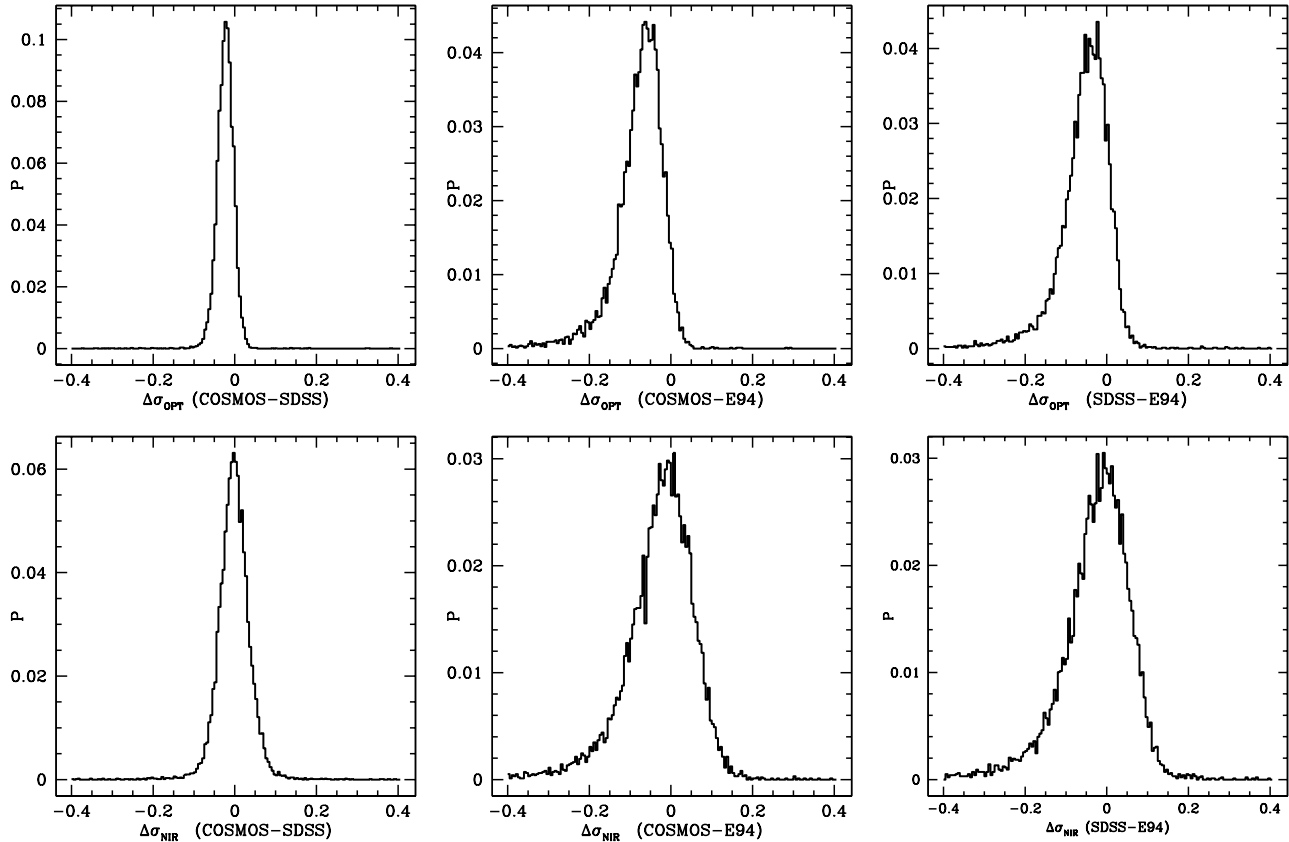


**Figure 4.** The probability distribution of the difference in slope dispersion in the three samples: *top*: optical slopes; *bottom*: near-infrared slopes.

ability distributions of the differences in slope dispersion between the samples are shown in Figure 4. For the dispersion in  $\alpha_{\text{OPT}}$ , the significance of the difference between the XMM-COSMOS and R06 sample is  $0.16\sigma$ ; between XMM-COSMOS and E94 sample is  $0.11\sigma$  and between R06 and E94 sample is  $0.08\sigma$ . Therefore, the intrinsic dispersions of the  $\alpha_{\text{OPT}}$  are consistent with being the same for all the three samples. For  $\alpha_{\text{NIR}}$ , the significance of the difference between the XMM-COSMOS and R06 sample is  $0.02\sigma$ ; between the XMM-COSMOS and E94 sample is  $0.08\sigma$  and between the R06 and E94 sample is  $0.06\sigma$ . As in the simpler analysis, the intrinsic dispersions of the  $\alpha_{\text{OPT}}$  and  $\alpha_{\text{NIR}}$  are consistent with being the same for all the three samples.

Using this result we can create a more rigorous AGN-dominated sample using the intrinsic dispersion to define a radius in the  $(\alpha_{\text{OPT}}, \alpha_{\text{NIR}})$  plane within which such AGN must lie. As the distribution of the quasars is continuous, different radii define different populations of quasars. We define a circle centered on the E94 RQ mean SED template with a radius of 0.6 on the mixing diagram to define AGN-dominated sources. This is approximately  $3\sigma_{\text{OPT}}$  and  $1.5\sigma_{\text{NIR}}$  of the intrinsic dispersion. For the XC413 sample, the sources within the dispersion circle populate mainly the left upper quadrant, similar to the R06 sample, but unlike the host corrected E94 sample. We will discuss this more in section § 4.1.

#### 4 APPLICATION OF THE MIXING DIAGRAM FOR XC413 SAMPLE

##### 4.1 SED Evolution on the Mixing Diagram

Hao et al. (2012a, Paper II) studied the evolution of the mean and dispersion of the SED with physical parameters (redshift  $z$ , bolometric luminosity  $L_{\text{bol}}$ , black hole mass  $M_{\text{BH}}$ , and accretion rate  $\lambda_E$ <sup>2</sup>) for the 407 radio quiet quasar in the XC413 sample. Paper II showed that there is no obvious evidence for evolution of the quasar SED shape with respect to these parameters. The study was limited by the difficulties of host galaxy subtraction. The conclusions are fully based on the assumption that host galaxy correction according to the black hole mass and bulge mass scaling relationship is reliable. The mixing diagram is a new tool to address this issue, with no need to rely on the assumption that the host correction is properly done. That is because the diagram itself can clearly show the contribution from the host galaxy.

In order to search for quasar SED evolution with respect to physical parameters, we plotted the mixing diagram for the XC413 sample in bins of  $z$ ,  $L_{\text{bol}}$ , and for the SS206 sample with two additional parameters  $M_{\text{BH}}$  and  $\log\lambda_E$ , because the black hole mass estimates are only available for these 206

<sup>2</sup>  $\lambda_E = \frac{L_{\text{bol}}}{L_{\text{Edd}}} = \frac{L_{\text{bol}}}{\frac{4\pi G c m_p}{\sigma_e} M_{\text{BH}}} = \frac{L_{\text{bol}}}{1.26 \times 10^{38} (M_{\text{BH}}/M_{\odot})}$

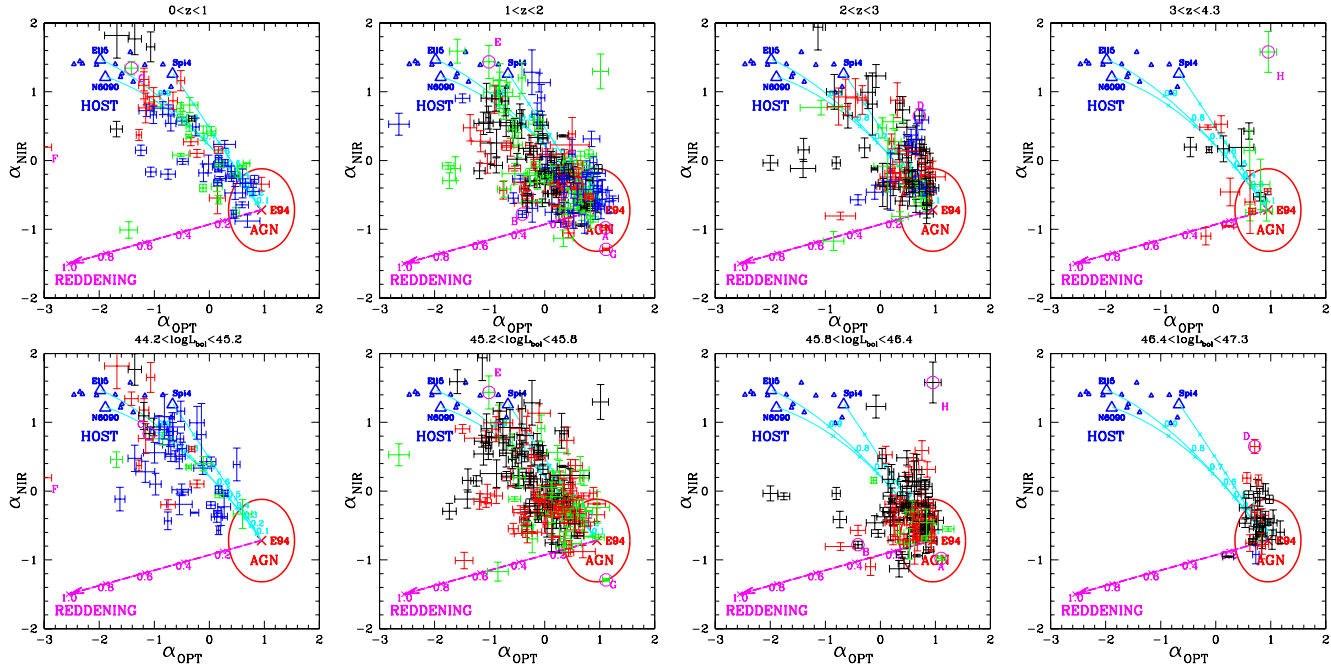


**Figure 5.**  $\alpha_{\text{NIR}}$  v.s.  $\alpha_{\text{OPT}}$  plot for the XC413 sample in  $z$  bins  $[0 - 1 - 2 - 3 - 4.3]$  (top row) and  $\log L_{\text{bol}}$  bins  $[44.2 - 45.2 - 45.8 - 46.4 - 47.3]$  (bottom row). Different colors of the points in each plot represent quasars in different sub-bins, with bin width 0.25, from low to high: black, red, green and blue. The E94 mean SED is shown as the red cross, with the galaxy templates from the SWIRE (Polletta et al. 2007, blue triangles). The cyan lines are the quasar-host mixing curves. The purple line is the reddening vector. The red circle shows the dispersion circle.

quasars in XC413 (see § 3.1). We divided the sample in four bins: in  $z$   $[0 - 1 - 2 - 3 - 4.3]$ , in  $L_{\text{bol}}$   $[44.2 - 45.2 - 45.8 - 46.4 - 47.3]$ , in  $M_{\text{BH}}$   $[7.1 - 7.7 - 8.3 - 8.9 - 9.4]$ , and in  $\log \lambda_E$   $[-1.9 - -1.2 - -0.6 - 0 - 0.7]$ , respectively. For each physical parameter the four bins have approximately equal bin size, so it is easy to compare bins. The resulting mixing diagrams are shown in Figures 5 and Figure 6.

To look for any SED evolution in smaller steps, we color coded the quasars in each bin for four equal sub-bins. In each  $z$  and  $\log L_{\text{bol}}$  mixing diagram, the black, red, green, and blue points represent quasars with small to large  $z$  and  $\log L_{\text{bol}}$ , with the sub-bin size of 0.25. Similarly, in each  $\log M_{\text{BH}}$  and  $\log \lambda_E$  mixing diagram, the black, red, green and blue colors represent small to large values, with sub-bin size of 0.15.

For the lowest bin of each parameter, almost all of the sources lie within the mixing wedge defined by the AGN-host mixing curve, allowing for the  $1\sigma$  range of the E94 mean SED slope, mixing curve and the reddening curve.

For high values of each parameter, the quasars cluster close to the quasar dominated region, while in the lower value bins the quasars spread out along the mixing curves toward the galaxy template locations. This effect is the strongest in  $L_{\text{bol}}$  bins. For different  $L_{\text{bol}}$  bins, the cluster of quasar locations clearly drifts along the mixing curves, from completely outside the AGN-dominated circle at low  $L_{\text{bol}}$ , with many sources lying near the pure galaxy-dominated region, to almost completely inside the dispersion circle at high  $L_{\text{bol}}$ . This is expected, as the galaxy luminosity is generally no more than  $10^{45}$  erg/s (Cirasuolo et al. 2007). Thus for extremely high luminosity sources, the AGN outshines the galaxy, especially in the optical. However, the  $M\text{-}\sigma$  re-

lation puts a limit on how much a quasar can outshine its host galaxy (Paper I, II).

Although almost all of the highest luminosity quasars lie within the AGN-dominated circle, they are not centered at the E94 RQ mean. Instead they lie overwhelmingly in the upper left quadrant of the dispersion circle, similar to the R06 sample as shown in the left panel of Figure 3. This suggests that some shift with respect to the E94 SED is present in both spectral slopes. For these highest luminosity quasars, the mean  $\alpha_{\text{OPT}}$  is 0.76, versus 0.95 for E94 mean SED, with  $\sigma = 0.18$ ; and the mean  $\alpha_{\text{NIR}}$  is -0.44, versus -0.72 for E94 mean SED, with  $\sigma = 0.30$ . In XC413 the slopes of the highest luminosity quasars are shifted by  $\sim 1\sigma$  relative to the E94 RQ mean SED. This may be an intrinsic shift, or may indicate a non-negligible host galaxy component even in these luminous quasars.

To compare in detail the highest luminosity quasars in XC413 and E94, we checked the 8 E94 quasars which lie in the same highest luminosity range (above  $2 \times 10^{46}$  erg/s). The mean  $\alpha_{\text{OPT},\text{E94}}$  of these 8 high luminosity E94 quasars is 0.93 with  $\sigma = 0.26$ , almost exactly the same as the optical slope of E94 mean SED, bluer ( $\sim 1\sigma$ ) than the XC413 high luminosity quasars. Instead, the mean  $\alpha_{\text{NIR},\text{E94}}$  of these 8 E94 quasars is -0.19, with  $\sigma = 0.38$ , which is much flatter than the NIR slope of E94 mean SED, and even flatter than the XC413 high luminosity quasars. This difference is mainly due to the two hot-dust-poor quasars in these 8 E94 quasars (Hao et al. 2011). From this comparison, we can only conclude that the highest luminosity E94 quasars are bluer than the highest luminosity XC413. We are not sure if this result can be explained by selection effects only.

In the higher  $z$  bins, a population of outliers is present

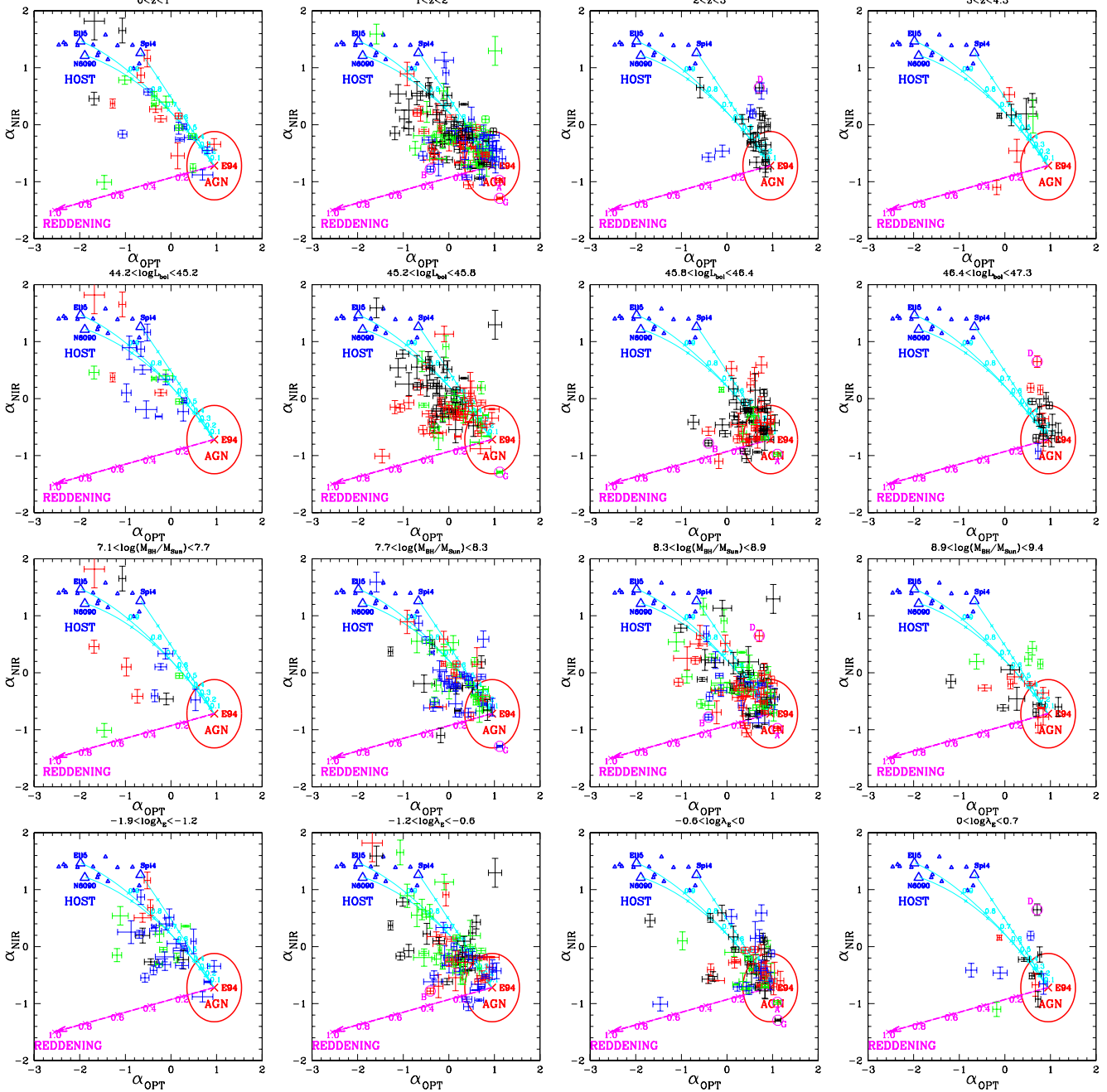


**Figure 6.**  $\alpha_{\text{NIR}}$  v.s.  $\alpha_{\text{OPT}}$  plot for SS206 sample in  $z$  bins  $[0 - 1 - 2 - 3 - 4.3]$  (top row),  $\log L_{\text{bol}}$  bins  $[44.2 - 45.2 - 45.8 - 46.4 - 47.3]$  (second row),  $\log(M_{\text{BH}}/M_{\text{Sun}})$  bins  $[7.1 - 7.7 - 8.3 - 8.9 - 9.4]$  (third row) and  $\log \lambda_E$  bins  $[-1.9 - -1.2 - -0.6 - 0 - 0.7]$ . Different color of points in each plot represent quasars in different sub-bins, with sub-bin width 0.25 for  $z$  and  $L_{\text{bol}}$  bins and sub-bin width 0.15 for  $M_{\text{BH}}$  and  $\lambda_E$  bins, from low to high: black, red, green and blue. The plots are color-coded as in Figure 5.

toward the top right corner. These outliers are the hot-dust-poor (HDP) quasars discussed in detail in Hao et al. (2010, 2011). The fraction of sources outside the mixing wedge is quite similar in the top three  $L_{\text{bol}}$ ,  $M_{\text{BH}}$  and  $\lambda_E$  bins. This result agrees with the lack of evolution in HDP fraction with  $M_{\text{BH}}$  and  $\lambda_E$  (Hao et al. 2010, 2011).

In first approximation, the contrast between nuclear AGN continuum and host galaxy in B band can be expressed

in a single formula (Merloni & Heinz 2012):

$$\frac{L_{\text{AGN},B}}{L_{\text{host},B}} = \frac{\lambda_E}{0.1} \frac{(M_*/L_B)_{\text{host}}}{3(M_{\odot}/L_{\odot})} (B/T),$$

where  $(M_*/L_B)_{\text{host}}$  is the mass-to-light ratio of the host galaxy and  $(B/T)$  is the bulge-to-total galactic stellar mass ratio. So for typical mass-to-light ratios and bulge-to-total galactic stellar mass ratios, the contrast will be smaller if  $\lambda_E$  is smaller, hinted as shown in the bottom row of Figure 6, from left to right. When  $\lambda_E$  is getting larger, the

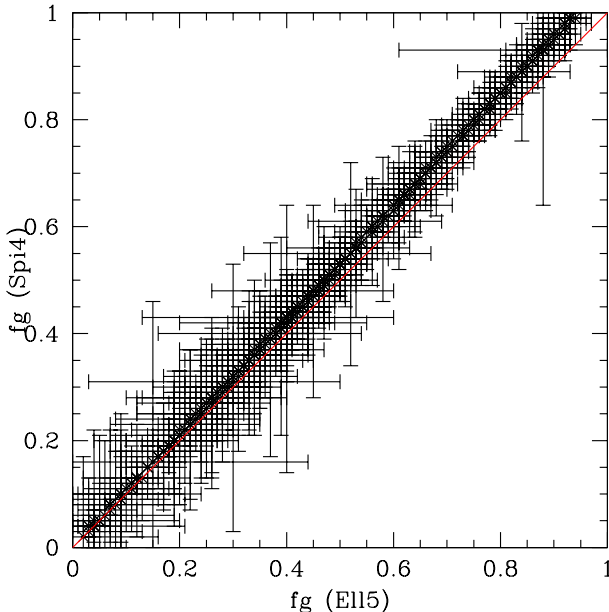


**Figure 7.** The  $f_g$  value of the XMM-COSMOS sample using the 5 Gyr elliptical galaxy template (Ell5) and the spiral galaxy (Spi4) from SWIRE template library (Polletta et al. 2007). The red solid line shows the one-to-one relation.

quasars generally drift towards the quasar dominated direction (smaller  $f_g$ ).

A minority of XC413 quasars in each of the lower bins of  $z$ ,  $L_{bol}$  lie in the highly reddened region ( $E(B-V) > 0.4$ ). For example, for the lowest  $z$  bin, the fraction is 6% (4 out of the 71 sources). In SS206, quasars in the highly reddened region only exists in the lower bins of  $z$  and  $L_{bol}$ . This effect is not so evident in  $M_{BH}$  and  $\lambda_E$ , where a small fraction of highly reddened quasars appear in high  $M_{BH}$  or  $\lambda_E$  bins. Extremely low Eddington ratio AGN ( $\lambda_E < 10^{-4}$ ) tend to have red optical SED, unlike the typical quasars ( $\lambda_E > 0.01$ ) with “big-blue-bump” (Ho et al. 2008, Trump et al. 2011). In SS206, we do not see any obvious trend that small Eddington ratio quasars are more reddened for the typical quasars.

## 4.2 Inferred Host Galaxy Fraction

The mixing diagram provides a new estimate of the galaxy fraction  $f_g$  (§ 2.2). The errors on the  $f_g$  estimates are caused by the error on the slopes, due to linear fitting of the SEDs. Different galaxy templates give slightly different  $f_g$  values. Figure 7 compares the values for two templates. The differences are negligible and almost unbiased, compared to the errors on  $f_g$ .

We can compare  $f_g$  with host galaxy fractions derived with two other methods: using bulge - black hole scaling relations and direct imaging. The two methods are briefly described below:

(1) *Black hole mass - Galaxy bulge scaling relations:* For the 203 quasars in SS206, following Paper I, we used the relationship between the black hole mass and near-infrared bulge luminosity (Table 2 of Marconi & Hunt, 2003) adding an evolutionary term (Bennert et al. 2010, 2011) to estimate

the host galaxy contribution:

$$\begin{aligned} \log(L_{J,Gal}) = & 0.877 \log(L_{bol}) + 3.545 - 0.877 \log \lambda_E \\ & - 1.23 \log(1+z) \end{aligned} \quad (1)$$

We used the Ell5 galaxy template to calculate the rest frame  $1\mu m$  host luminosity. In this band the differences among different galaxy templates are small. With the host luminosity we can calculate the galaxy fraction at rest frame  $1\mu m$  ( $f_{g,MH}$ ). The rest frame J band ( $1.2\mu m$ ) luminosity  $L_{J,gal}$ , was used because this is the band closest to  $1\mu m$ , and is where the galaxy contribution peaks.

The small photometric errors in J imply that black hole mass measurement errors dominate the error on  $f_{g,MH}$ . Black hole mass estimates from mass scaling relationships have an error  $\Delta M_{BH}/M_{BH} \sim 40\%$  (Vestergaard & Peterson 2006; Peterson 2010), so  $\Delta f_{g,MH}/f_{g,MH} \sim 35\%$ , as  $f_{g,MH} \propto M_{BH}^{0.877}$  (according to Equation 1).

(2) *Direct imaging:* For 94 low redshift ( $z \lesssim 1.2$ ) quasars in the XMM-COSMOS sample, Cisternas et al. (2011) used the Hubble images to decompose the AGN and galaxy emission and to estimate the host galaxy fraction at  $8140\text{\AA}$  (observed frame). We transformed this galaxy fraction to the rest frame  $1\mu m$  galaxy fraction ( $f_{g,C}$ ) using the Ell5 galaxy template. As only the best fit model of the host galaxy luminosity is given, we cannot estimate the error on  $f_{g,C}$  due to the fitting process.

However, the assumed template introduces an uncertainty. The observed F814W photometry point lies on the steep side of the galaxy template for  $z > 0.1$ . Hence, a small error in template slope (or, effectively, in the age of the youngest stellar population in the host) would lead to a large error in the host estimate at  $1\mu m$ . We can use this extrapolation uncertainty to estimate a minimum error. To do so, we normalized the 16 SWIRE galaxy templates (Polletta et al. 2007) at  $1\mu m$  and measured the dispersion of these different templates at the rest frame wavelength corresponding to the observed  $8140\text{\AA}$ . We use these dispersions as errors on the host galaxy luminosities  $L_{g,C}$  at  $1\mu m$  for sources at different redshifts. Therefore, the error on the galaxy fraction can be estimated as  $\Delta f_{g,C}/f_{g,C} = \Delta L_{g,C}/L_{g,C}$ . The error bar ranges from 0.02 to 0.77 with the median value of 0.21.

The comparison of  $f_g$  estimated from the mixing diagram with the galaxy fraction from the other two methods  $f_{g,MH}$  (from Paper I) and  $f_{g,C}$  (from Cisternas et al. 2011) is shown in the top row of Figure 8. The three methods give values which are poorly correlated. The correlation coefficient for  $f_g$  and  $f_{g,MH}$  is 0.34, for  $f_g$  and  $f_{g,C}$  is -0.11 and for  $f_{g,MH}$  and  $f_{g,C}$  is -0.18. It is not possible to tell which method works the best. However,  $f_{g,MH}$  seems to give systematically smaller values than the other two methods.

The inferred host galaxy luminosities ( $L_g$ ,  $L_{g,MH}$  and  $L_{g,C}$ ) are also compared in Figure 8 (bottom row). These show a hint of correlation, which is somewhat encouraging. For most of the cases the inferred host galaxy luminosity  $\nu L_\nu$  is less than  $10^{44.6}\text{erg/s}$  (that is  $M > -23$ ), a reasonable value, as  $M_K^* = -23$  (Cirasuolo et al. 2007).

Using the mixing diagram to estimate the host galaxy fraction implies the following the assumptions: 1) an intrinsic quasar SED exists and it is similar to E94 mean SED; 2) all the quasars have a similar reddening curve which is SMC like. The first assumption is somewhat reasonable based on

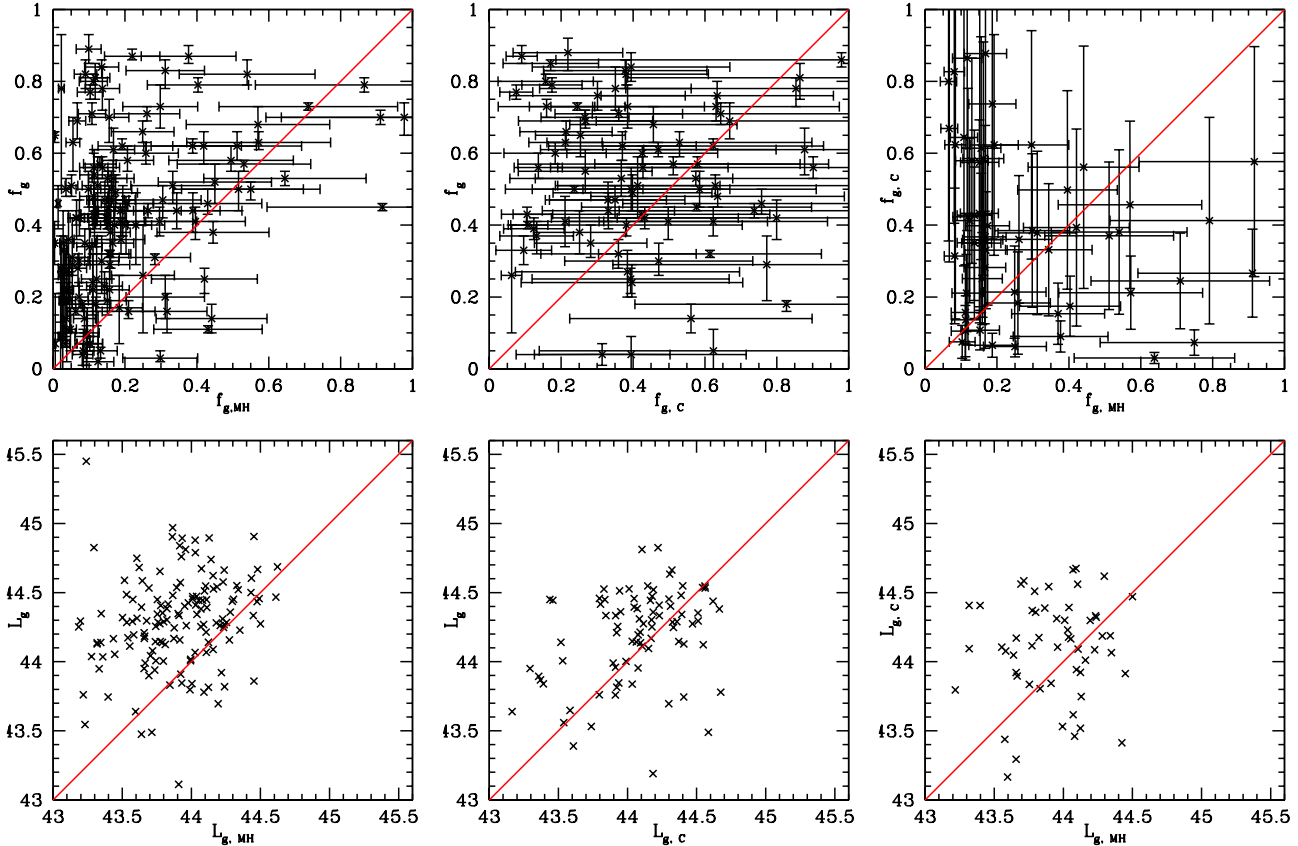


**Figure 8.** The comparison of the galaxy fraction (top) and host galaxy luminosity (bottom) of the XMM-COSMOS sample at rest frame  $1\mu\text{m}$ : (1) from the mixing diagram, (2) from the Marconi & Hunt (2003) scaling relationship adding an evolutionary term (Bennert et al. 2010, 2011), and (3) from the Hubble image decomposition (Cisternas et al. 2011). The red solid line shown the one-to-one relation.

the dependency studies of mean SEDs with physical parameters (Paper II) and § 3.3 in this paper. The reliability of the second assumption is somewhat difficult to answer. As we have already shown in Figure 7, the difference in the galaxy templates has little effects to the host galaxy estimation in this method. Estimation of the host galaxy fraction using the scaling relationship has a large uncertainty due to the dispersion of the relationship itself (e.g. Marconi & Hunt 2003) and possible evolution in the relationship (e.g. Merloni et al. 2010). The error of the host galaxy fraction at certain rest frame wavelength (e.g.  $1\mu\text{m}$ ) mainly comes from the large varieties of the galaxy SED itself (e.g. Polletta et al. 2007). Thus comparing the estimations of the host galaxy fraction or host galaxy luminosity from these methods is rather difficult, and we defer the detailed analysis to future papers.

#### 4.3 Inferred Reddening

In addition to the galaxy fraction estimation, from the mixing diagram we could get an estimation of the  $E(B-V)$  value from the position of the source on the mixing diagram (§ 2.2). The errors on the  $E(B-V)$  estimates are also caused by the error on the slopes due to linear fitting of the SEDs similar to the  $f_g$  estimates. Different galaxy templates give different  $f_g$  values. Figure 9 compares the values  $E(B-V)$  for two templates. Compared to  $f_g$  estimates, the  $E(B-V)$  estimates are more affected by which galaxy template is chosen.

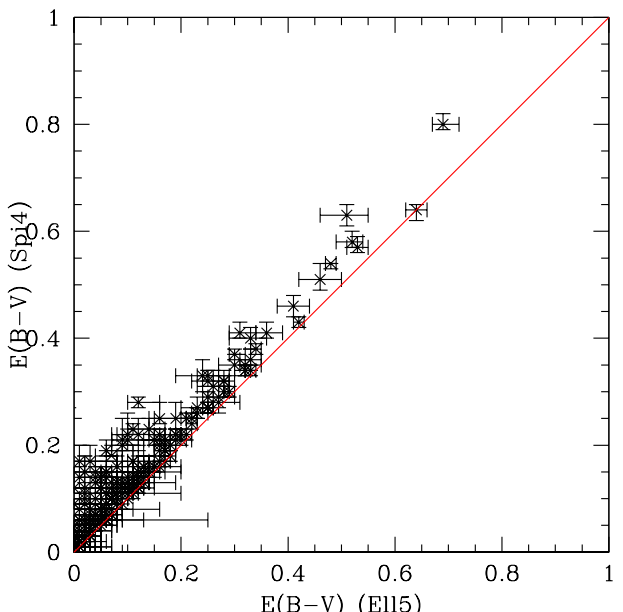


**Figure 9.** The  $E(B-V)$  estimates of the XMM-COSMOS sample using the 5 Gyr elliptical galaxy template (Ell5) and the spiral galaxy (Spi4) from SWIRE template library (Polletta et al. 2007). The red solid line shows the one-to-one relation.

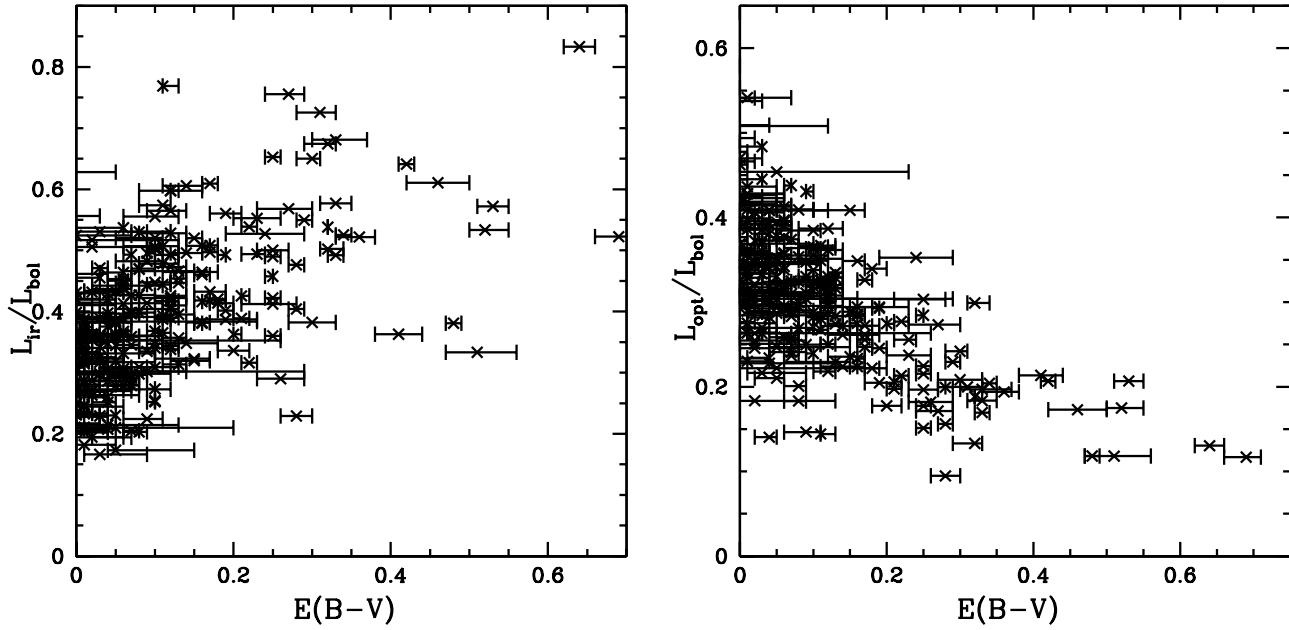


Figure 10. The NIR luminosity fraction versus  $E(B-V)$  (left) and the optical luminosity fraction versus  $E(B-V)$  (right).

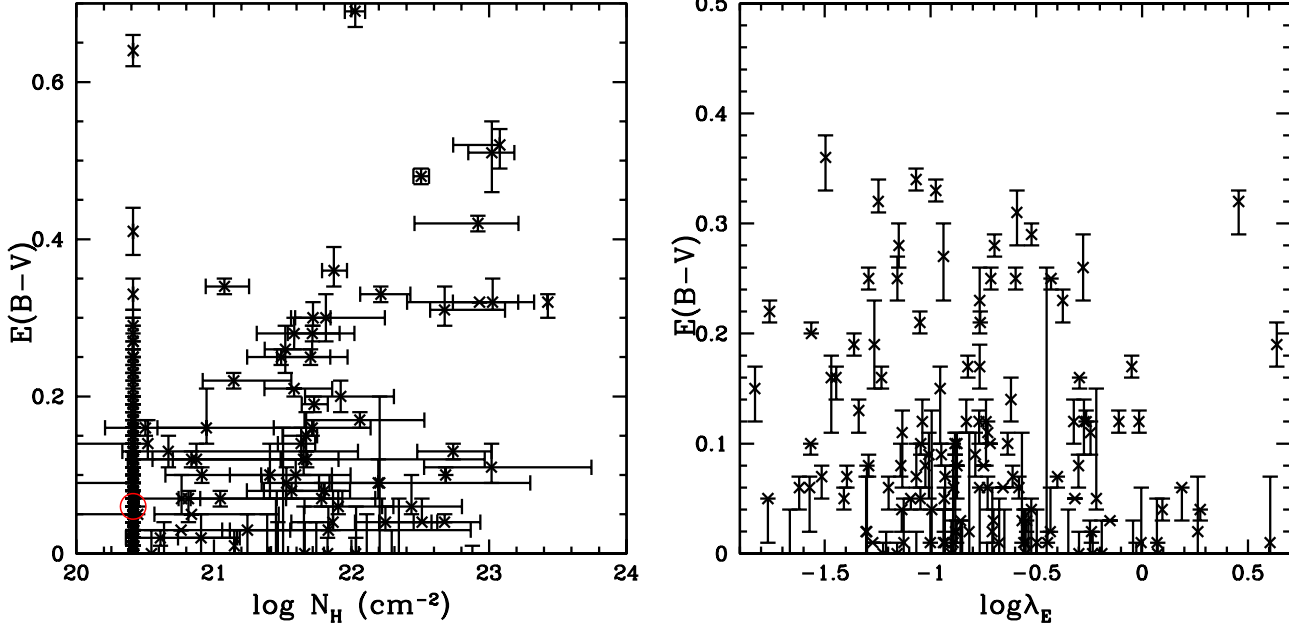


Figure 11. The  $E(B-V)$  versus the neutral Hydrogen column density  $N_H$  (left) and  $E(B-V)$  versus Eddington Ratio  $\log \lambda_E = \log(L_{bol}/L_{Edd})$  (right). The red circle in the left panel shows the median  $E(B-V)$  ( $=0.06$ ) of the AGN with no intrinsic  $N_H$ .

This is expected as the galaxy templates are distributed in a sparse region on the upper left part of the mixing diagram. Thus, the mixing curves for different templates would spread out in the large  $f_g$  direction, leading to large difference of the  $E(B-V)$  estimates for the same quasar.

According to definition, the  $E(B-V)$  is generally estimated by applying a standard extinction law to an assumed intrinsic optical-to-NIR quasar SED template (e.g. Vasudevan et al. 2009, Glikman et al. 2012). Here the SMC extinc-

tion curve is chosen because the extinction curve of quasars is generally believed to be better described by the SMC type (Hopkins et al. 2004; Gallerani et al. 2010). The  $E(B-V)$  estimation derived from the mixing diagram is equivalent to assuming the E94 template as an intrinsic quasar template and applying the SMC reddening law. As E94 template is the mean SED of the bright quasar sample, and for each quasar in the E94 sample the possible reddening is not corrected, we are expecting the E94 template to be slightly

redder than the intrinsic quasar SED. In this case, the E(B-V) estimation derived from the mixing diagram should be a lower limit. As a fraction of the quasars lies in the upper right corner beyond the mixing curve leading to negative E(B-V) values, we ignore these quasars from further discussion in this section. The size of the fraction clearly depend on the mixing curve chosen to derived the E(B-V) values.

Other than estimate the E(B-V) from the optical-to-NIR SED, Balmer decrements have been used historically to estimate the reddening along the line of sight of quasars (e.g., Maiolino et al. 2001, Xiao et al. 2012). However, this method requires spectra that include both the H $\alpha$  and H $\beta$  lines, which is not suitable for the XMM-COSMOS sample, because most of the quasars are at redshifts around 1–2. Besides, Glikman et al. (2012) argued that using the optical-to-NIR SED to estimate the reddening is much more reliable than the Balmer decrements estimation.

Other independent estimates of E(B-V) are very difficult. The galaxy inclination derived from HST images or the total dust masses estimated from the infrared luminosity might give a hint to how much reddening we would expect, but to get E(B-V) estimates by these methods would require lots of assumption on the gas and dust content of the host galaxy. Thus, it is very difficult to compare the E(B-V) values derived from the mixing diagram with those from other measurements to test the reliability of the mixing diagram. In general, we would expect that for quasars with high E(B-V) values, the infrared bump would be more prominent and the ‘big-blue-bump’ would be less prominent. We check the correlation of the NIR luminosity fraction ( $L_{\text{ir}}/L_{\text{bol}}$ , where  $L_{\text{ir}}$  is the luminosity integrated from rest-frame  $24\mu\text{m}$  to  $1\mu\text{m}$ , Paper II) and the optical luminosity fraction ( $L_{\text{opt}}/L_{\text{bol}}$ , where  $L_{\text{opt}}$  is the luminosity integrated from rest-frame  $1\mu\text{m}$  to  $912\text{\AA}$  Paper II) with E(B-V) respectively (Figure 10). In Figure 10, we compare the optical and NIR luminosity fraction with the E(B-V) values derived from the Ell5 mixing curve as an example. For the 226 quasars with positive E(B-V) values from the Ell5 mixing curve, the correlation coefficient for the NIR luminosity fraction with E(B-V) is 0.54 and for the optical luminosity fraction with E(B-V) is -0.62. So the optical and NIR luminosity fractions with E(B-V) are correlated as expected.

The neutral Hydrogen column density ( $N_{\text{H}}$ ) estimated from the X-ray spectrum is usually used as an indicator of the absorber. However, the optical and X-ray obscuration are caused by different physical processes and thus can be very different in an object (e.g. Crenshaw & Kraemer 2001). We checked the estimated E(B-V) versus  $N_{\text{H}}$  (Mainieri et al. 2007) for the XMM-COSMOS sample (Figure 11 left). For the 413 quasars in XMM-COSMOS sample, 378 quasars have good enough XMM spectrum to do a fitting. In 273 out of the 378 cases, no intrinsic  $N_{\text{H}}$  is necessary from the spectrum, so the  $N_{\text{H}}$  value is set to the Galactic  $N_{\text{H}}$  in the COSMOS region ( $\log N_{\text{H}} = 20.413 \text{ cm}^{-2}$ ). The correlation coefficient of the E(B-V) derived from the mixing diagram and  $N_{\text{H}}$  fitted from the X-ray spectra is 0.40. Note that we only choose the 205 quasars with a  $N_{\text{H}}$  estimate and positive E(B-V) value for this correlation coefficient calculation. Formally, a correlation coefficient 0.40 with 205 objects corresponds to a significant correlation (at  $>5\sigma$  level) between  $N_{\text{H}}$  and E(B-V). As shown in the Figure 11 (left), there is

however a large dispersion with some potentially interesting outliers, e.g. objects with no intrinsic  $N_{\text{H}}$  and high E(B-V).

Low accretion rate ( $\lambda_E \lesssim 10^{-4}$ ) quasars have more reddened ‘big-blue-bump’ (e.g. Ho 2008, Trump et al. 2011). We checked the estimated E(B-V) versus the accretion rate ( $\lambda_E$ ) in Figure 11 (right) to see if we see a similar trend in XMM-COSMOS sample. The correlation coefficient between E(B-V) and  $\log \lambda_E$  is -0.035 for the 119 quasars with  $\log \lambda_E$  estimates and positive E(B-V) estimates, thus no correlation is observed. The studies of Fabian et al. (2008, 2009) identify the effective Eddington limit for dusty gas in the  $N_{\text{H}} - \lambda_E$  plane, and therefore causing a ‘forbidden region’ in the  $N_{\text{H}} - \lambda_E$  space within which absorbing dusty gas clouds are unstable to radiation. Vasudevan et al. (2009) shows a similar ‘forbidden region’ in the upper right corner of the E(B-V) –  $\lambda_E$  plane. In the right plot of Figure 11, we can see a similar ‘forbidden region’ in the upper right corner as in Vasudevan et al. (2009).

#### 4.4 Identify Outliers

There are sources lying outside the mixing wedge. All of them are candidate outliers with respect to the bulk of the type 1 AGN population. As noted above (§ 4.1), the mixing diagram has already been successfully used to identify a population of HDP quasars lacking the characteristic maximally hot dust of AGN (Hao et al. 2010, 2011).

Four extreme examples of SEDs singled out in Paper I (A, B, C, D) are also marked in Figure 2. They lie at the four corners of the mixing diagram. Figure 12 displays the SEDs of four additional outliers (E, F, G, H) which are discussed briefly below. These four quasars lies in the furthest corners of the mixing diagram. A detailed discussion will be deferred to later papers.

- *A New Born quasar?* Object E (XID=304, COSMOS\_J095931.58+021905.52,  $z=1.607$ ) has a SED well fit by the ULIRG Arp 220 SED (Polletta et al. 2007) at  $\lambda > 0.40\mu\text{m}$ . However, in the UV (at  $\lambda < 0.40\mu\text{m}$ ), a weak quasar component emerges, as do the broad emission lines that identify it as a type 1 AGN. This object has a luminosity in the ULIRG regime (the bolometric luminosity integrated in  $24\mu\text{m} - 40 \text{ keV}$  range is  $10^{12.2} L_{\odot}$ ) and appears to be a composite quasar/starburst. The rarity of objects like it in XMM-COSMOS argues for a short-lived phase. Object E is thus a good candidate for a newly born quasar, or at the beginning of the “buried quasar stage”, where the quasar emerges during a merger triggered starburst (Hopkins et al. 2006). The obscured starburst activity still dominates the SED and the quasar is still too weak to quench the starburst activity.

- *A Weak Big Blue Bump Quasar?* Object F (XID=135, COSMOS\_J095848.21+022409.3,  $z=0.376$ ) shows a two dex drop in the u-band compared to the E94 RQ mean SED. An extinction of E(B-V)=0.8 could be applied. This source is classified as type 1 AGN because a strong broad H $\alpha$  line (FWHM $\sim 5000\text{km/s}$ ) is present in the optical spectrum. Can there be strong differential reddening between the continuum and the broad line emitting region? Alternatively, an NGC 6090 template fits the optical/UV SED well. Is then the UV ‘big blue bump’ intrinsically weak in this object?

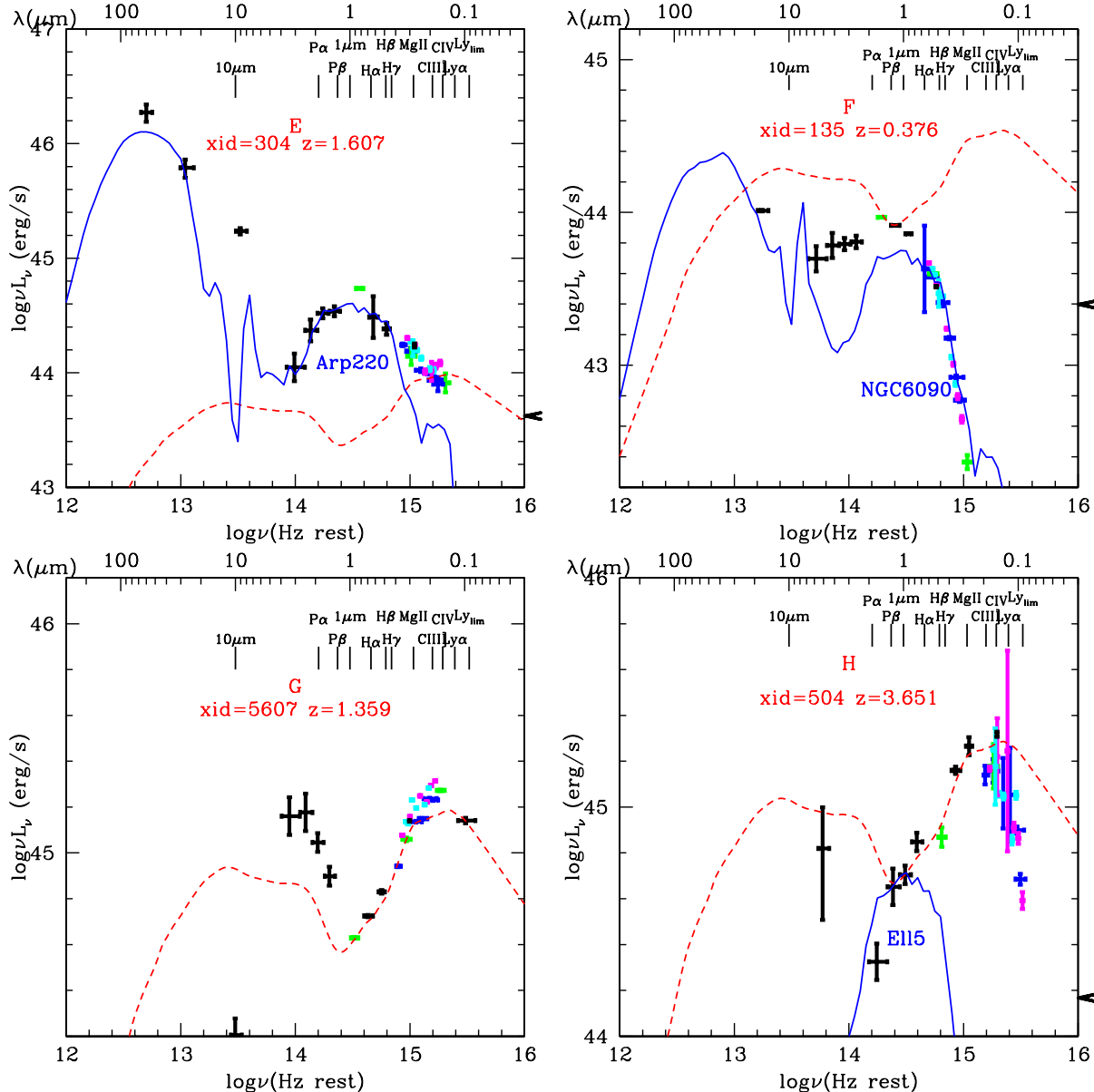


**Figure 12.** Extreme examples of SEDs: *top left*: E. a close analog of a ULIRG SED, with prominent infrared emission; *top right*: F. no big blue bump, probably due to extreme reddening; *bottom left*: G. big near-infrared bump, due to rich hot dust emission; *top right*: H. hot-dust-poor quasar, strong big blue bump but no  $1\ \mu\text{m}$  inflection due to a weak near-IR bump. The red dashed line is the E94 RQ mean SED. The blue lines are the galaxy templates (Polletta et al. 2007). The data points in the SED are color-coded as in Elvis et al. (2012). From low frequency to high frequency, the black data points are:  $24\ \mu\text{m}$ ,  $8\ \mu\text{m}$ ,  $5.7\ \mu\text{m}$ ,  $4.5\ \mu\text{m}$ ,  $3.6\ \mu\text{m}$ , K-band, H-band, J-band, the NUV and FUV. The blue data points are the Subaru broad bands (B, g, r, i, z) from 2005. The green data points are the (CFHT) K-band, and the (CFHT) u band and i band. The purple data points are the 6 Subaru intermediate bands for season 1 (2006) (IA427, IA464, IA505, IA574, IA709, IA827). The cyan data points are the 5 Subaru intermediate bands for season 2 (2007) (IA484, IA527, IA624, IA679, IA738, IA767).

The high X-ray flux relative to the optical would make for a truly unusual SED in the extreme UV.

- A “Blow-out” Phase Quasar? Object G (XID = 5607, COSMOS\_J 095743.33+024823.8,  $z=1.359$ ) is well fitted by the E94 RQ mean SED in the optical/UV, but shows an unusually strong near-infrared bump, two times brighter than the E94 RQ mean SED at  $3\ \mu\text{m}$ , indicating an unusually rich hot dust component. Such a quasar could be a good candidate for objects at the end of the “buried quasar stage” or the beginning of the “blow out phase”, where the quasar

emerges from its dusty cocoon and begins to dominate the SED (Hopkins et al. 2006). The properties of these quasars still need to be investigated.

- Hot Dust Poor Quasar Object H (XID=504, COSMOS\_J 095931.01+021333.0,  $z=3.651$ ) is located in the upper right corner, furthest from the E94 mean SED template in the mixing diagram of the XC413 sample. The SED of object H has a typical strong big blue bump but weak infrared emission. that is another hot-dust-poor quasar as source D described in Paper I, and discussed in detail in Hao et al.

(2010). They could be sources that used up or blow-out most the dust and gas.

## 5 DISCUSSION AND CONCLUSIONS

Making use of the strong SED shape differences around  $1\mu m$  for galaxies and quasars, we defined the quasar-galaxy mixing diagram: a plot of the  $1 - 3\mu m$  SED slope versus the  $0.3 - 1\mu m$  SED slope. This diagram allows us to easily distinguish among quasar-dominated, galaxy-dominated and reddening-dominated SEDs without making strong model assumptions.

This mixing diagram, when applied to the XMM-COSMOS sample shows that  $\sim 90\%$  of the quasar SEDs can be explained by the combination of (1) an E94-like mean SED, (2) a host galaxy SED and (3) reddening.

Changes in the quasar SED shape with respect to the physical parameters  $z$ ,  $L_{bol}$ ,  $M_{BH}$  and  $\lambda_E$  were sought. At high  $z$ ,  $L_{bol}$ ,  $M_{BH}$  and  $\lambda_E$ , the XMM-COSMOS quasars cluster close to the E94 mean, with a slight offset, which could be due to either an intrinsic SED change, or a small but not negligible host galaxy component. Lower  $z$ ,  $L_{bol}$ ,  $M_{BH}$  and  $\lambda_E$  sources spread along the E94 mean SED - host mixing curves. The mixing diagram allows estimates of the galaxy fraction and the reddening for each AGN. Reddening of  $E(B-V) > 0.4$  is seen mainly among low  $z$ ,  $L_{bol}$  objects.

The galaxy fractions estimated from the mixing diagram were compared with those estimated both from the black hole mass - bulge mass scaling relationship and from direct Hubble image decomposition. The host fraction estimated from the three methods show weak correlation, though all have large errors. The black hole mass - bulge method seems to give systematically smaller galaxy fractions.

The reddening ( $E(B-V)$ ) estimated from the mixing diagram were correlated with the NIR luminosity ratio ( $L_{ir}/L_{bol}$ ) and OPT luminosity ratio ( $L_{opt}/L_{bol}$ ). A significant correlation is found for  $E(B-V)$  versus  $N_H$ , although with a large spread. The derived  $E(B-V)$  and  $\lambda_E$  are not significantly correlated. A ‘forbidden region’ in the  $E(B-V)$  versus  $\lambda_E$  space is seen as in Vasudevan et al. (2009).

The mixing diagram is also efficient at identifying outliers. These may represent different short stages of the quasar-galaxy co-evolution.

The mixing diagram can clearly distinguish among the quasar-dominated, host-dominated and reddening-dominated SEDs. Thus different phases of galaxy formation and evolution would locate in different regions of the diagram. A complete evolutionary track of the quasar-galaxy co-evolution cycle can, in principle, be drawn on the mixing diagram, by analogy to tracks in the HR diagram in stellar astrophysics. Numerical simulations have reproduced quasars at various redshifts from hierarchical assembly in the  $\Lambda$ CDM cosmology (Hopkins et al. 2006; Li et al. 2007), but have not addressed how the resulting SEDs change.

There are various different galaxy formation and evolution models. Two representatives would be 1) the ‘cosmic cycle’ (Hopkins et al. 2006) for galaxy formation and evolution, which are regulated by black hole growth in mergers; 2) the galaxy evolution triggered by self-regulated baryonic process (Granato et al. 2004). The main difference between

these two models is in the beginning phase: 1) in the merger-driven model (Hopkins et al. 2006), star-formation is enhanced by the merging of two late-type galaxies; 2) in the anti-hierarchical baryon collapse model (Granato et al. 2004) the proto-spheroidal galaxies formed in the virialized dark matter halo have high star-formation rate (Mao et al. 2007). The following black hole growth (Lapi et al. 2006, Hopkins et al. 2006) and galaxy evolution in both models are similar to each other with some difference in timescales of different phases. Thus in the mixing diagram, the evolutionary tracks between different models would be very similar in most regions.

A sketch of a possible evolutionary track is shown in Figure 13. Mergers drive a galaxy (1, red) into the starburst region (2, blue). Here, the SMBH grows by accretion. The quasar emission gradually comes to dominate the luminosity, but is ‘buried’ by gas and dust, so the source moves downward in the mixing diagram for the phase of obscured quasar activity (3, green). Sources in this stage would be identified as type 2 AGN, not included in the XC413 sample. At the end of this buried quasar phase, hot dust rich (HDR) quasars - the outliers with much stronger hot dust emission than typical quasar and broad emission lines - would be found at the very bottom of the mixing diagram. At this stage, feedback from the SMBH expels enough interstellar medium, and the obscuring ‘torus’ and the broad line region emission become visible, and the object gradually moves either from a ‘buried’ or ‘HDR’ quasar to the typical quasar region (4, purple) if the ratio between AGN and host galaxy luminosity is high. Lower luminosity AGN would move near the mixing curves. As the SMBH continues to accrete, the gas and dust is either used up as a reservoir, or expelled. The dust covering factor reduces, and the source moves up to the HDP quasar region, before finally becoming quiescent once more.

A family of possible evolutionary cycles could be drawn, varying the parameters of the initial merging (e.g. mass, gas fraction, accretion rate). A quantitative picture of the cosmic cycle (e.g. the duration of the duty cycle in each phase, the dependence on the initial conditions, etc.) could thus be obtained from the density of objects around the mixing diagram. These results, in turn, could put constraints on the physics adopted to model AGN/galaxy coevolution in numerical simulations. We plan to address the quantitative evolution of quasar-galaxy SEDs in the mixing diagram, over the complete cosmic cycle in later papers, including in the analysis of also type 2 AGN.

However, we have to note that Figure 13 is just an idealized illustration. The tracks of the evolution of sources could be very complicated and sources could just wandering around in the mixing region. Bongiorno et al. (2012) plotted all the XMM-COSMOS sources in the mixing diagram and there is no obvious accretion rate distribution correlated with different regions on the mixing diagram observed. We defer the study of the evolution tracks on the mixing diagram to a later paper.

For a longer term study of the full evolutionary picture, the mixing diagram definition could be extended to other wavelengths. For example, we could investigate the optical to ultraviolet SED with respect to the near infrared SED for the extinction law; we could study the radio and far-infrared SED with respect to optical/near-infrared for the

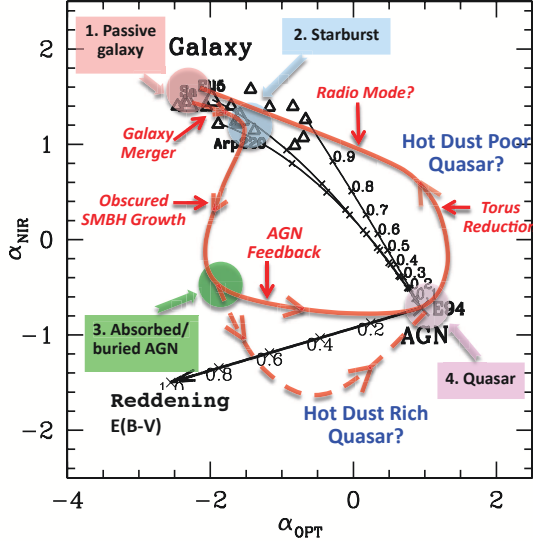


**Figure 13.** The evolution view of the mixing diagram. Four different phases of the “cosmic cycle” are shown as colored circles. The red line shows the evolution track of an AGN life cycle.

radio-loudness; we could check the ultraviolet SED with respect to X-ray for the  $\alpha_{OX}$ . The multiwavelength analysis of the AGN emission could not only significantly improve our understanding of the SMBH accretion, the AGN structure and the unification of AGN, but also would help us understand the role of the SMBH in the co-evolution cosmic cycle.

## ACKNOWLEDGMENTS

HH thanks Belinda Wilkes, Martin J. Ward and Zhenyi Cai for valuable discussions. This work was supported in part by NASA *Chandra* grant number G07-8136A (HH, ME, CV). Support from the Italian Space Agency (ASI) under the contracts ASI-INAF I/088/06/0 and I/009/10/0 is acknowledged (AC and CV). MS acknowledges support by the German Deutsche Forschungsgemeinschaft, DFG Leibniz Prize (FKZ HA 1850/28-1).

## REFERENCES

Barvainis, R. 1987, *ApJ*, 320, 537

Bennert, V. N., Treu, T., Woo, J.-H., Malkan, M. A., Le Bris, A., Auger, M. W., Gallagher, S., Blandford, R. D., 2010, *ApJ*, 708, 1507

Bennert, V. N., Auger, M. W., Treu, T., Woo, J.-H., Malkan, M. A., 2011, *ApJ*, 742, 107

Bongiorno, A. et al. 2007, *A&A*, 472, 443

Bongiorno, A. et al. 2012, *MNRAS* accepted (astro-ph/1209.1640)

Brandt, W. N. & Hasinger, G. 2005, *ARA&A*, 43, 827

Brusa, M., et al., 2007, *ApJS*, 2007, 172, 353

Brusa, M., et al., 2010, *ApJ*, 716, 348

Cappelluti, N., et al., 2007, *ApJS*, 172, 341

Cappelluti, N., et al., 2009, *A&A*, 497, 635

Cirasuolo, M. et al. 2007, *MNRAS*, 380, 585

Cisternas, M. et al. 2011, *ApJ*, 726, 57

Civano, F., et al., 2011, *ApJ*, 741, 91

Crenshaw D. M. & Kraemer S. B. 2001, *ApJ*, 562, L29

Elvis, M. et al., 1994, *ApJS*, 95, 1

Elvis, M. et al., 2011, *ApJ*, accepted, astro-ph/1209.1478

Fabian, A. C., Vasudevan, R. V., & Gandhi, P., 2008, *MNRAS*, 385, L43

Fabian, A. C., Vasudevan, R. V., Mushotzky, R. F., Winter, L. M., & Reynolds, C. S., 2009, *MNRAS*, 394, 89

Ferrarese, L. & Merritt, D. 2000 *ApJ*, 539, L9

Fitzpatrick, E. L. 1999, *PASP*, 111, 63

Franceschini, A., Hasinger, G., Miyaji, T., & Malquori, D., 1999, *MNRAS*, 310, L5

Gallerani, S., et al., 2010, *A&A*, 523, 85

Gebhardt, K., et al. 2000, *AJ*, 539, L13

Glikman, E., Helfand, D. J., & White, R. L., 2006, *ApJ*, 640, 579

Glikman, E., et al. 2012, *ApJ*, 757, 51

Gordon, K. et al., 2003, *ApJ*, 594, 279

Granato, G. L., De Zotti, G., Silva, L., Bressan, A., Danese, L., 2004, *ApJ*, 600, 580

Hao, H., et al., 2010, *ApJ*, 724, L59

Hao, H., et al., 2011, *ApJ*, 733, 108

Hao, H., et al., 2012a, *MNRAS* submitted

Hao, H., et al., 2012b, *ApJL* submitted

Hasinger, G., et al., 2007, *ApJS*, 172, 29

Ho, L. C., 2008, *ARA&A*, 46, 475

Hopkins, P. F., et al., 2004, *AJ*, 128, 1112

Hopkins, P. F., et al., 2006, *ApJS*, 163, 1

Jiang, L. et al., 2010, *Nature*, 464, 380

Kelly, Brandon C. 2007, *ApJ*, 665, 1489

Komatsu, E., et al., 2009, *ApJS*, 180, 330

Kormendy, J. & Richstone, D. 1995, *ARA&A*, 33, 581

Lapi, A., et al., *ApJ*, 650, 42

Li, Y., et al., 2007, *ApJ*, 665, 187

Lilly, S. J., et al., 2007, *ApJS* 172, 70

Lilly, S. J., et al., 2009, *ApJS* 184, 218

Mainieri, V., et al., 2007, *ApJS*, 172, 368

Maiolino, R., et al. 2001, *A&A*, 365, 28

Malkan, M. A., & Sargent, W. L. W., 1982, *ApJ*, 254, 22

Mao, J., Lapi, A., Granato, G. L., De Zotti, G., Danese, L., 2007, *ApJ*, 667, 655

Marconi, A. & Hunt, L. K. 2003, *ApJ*, 589, L21

McCracken, H. J., et al., 2010, *ApJ*, 708, 202

Merloni, A., et al. 2010 *ApJ* 708, 137

Merloni, A., & Heinz, S., 2012, *Planets, Stars and Stellar Systems*, vol 6, ed W. Keel

O’Brien, P. T., Wilson, R., & Gondhalekar, P. M. 1988, *MNRAS*, 233, 801

Polletta, M., et al. 2007, *ApJ*, 663, 81

Richards, G. T., et al. 2003, *AJ*, 126, 1131

Richards, G. T. et al. 2006, *ApJS*, 166, 470

Richstone, D., et al. 1998, *Nature*, 395, 14

Salvato, M. et al. 2009 *ApJ* 690, 1250

Sandage, A. 1971 SWNG conf, 271

Sanders, D. B., Phinney, E. S., Neugebauer, G., Soifer, B. T., & Matthews, K. 1989, *ApJ*, 347, 29

Schmidt, M. & Green, R. F. 1983, *ApJ*, 269, 352

Schneider, D. P. et al. 2007, *AJ*, 134, 102

Scoville, N. Z., et al., 2007, ApJS, 172, 1  
Shang, Zhaohui, et al., 2011, ApJS, 196, 2  
Sikora, M., Stawarz, L. & Lasota, J. P., 2007, ApJ, 658, 815  
Silva, L., Granato, G. L., Bressan, A., & Danese, L. 1998, ApJ, 509, 103  
Silverman, J. D. et al. 2005, ApJ, 624, 630  
Soltan, A., 1982, MNRAS, 200, 115  
Taniguchi, Y. 1999, ApJ, 524, 65  
Trump, J. R. et al. 2009 ApJ, 696, 1195  
Trump, J. R. et al. 2011 ApJ, 733, 60  
Vasudevan, R. V., Mushotzky, R. F., Winter, L. M., & Fabian, A. C. 2009, MNRAS, 399, 1553  
Vestergaard, M. & Peterson, B. M. 2006 ApJ 641, 689  
Ueda, Y. et al. 2003 ApJ 598, 886  
Ward, M. et al. 1987 ApJ, 315, 74  
Weedman, D. 1973 ApJ, 183, 29  
Wills, B. J., Netzer, H., & Wills, D. 1985, ApJ, 288, 94  
Xiao, T., et al. 2012, MNRAS, 421, 486  
Young, M., Elvis, M., & Risaliti, G. 2008, ApJ, 688, 128